20

In situ observations of the physical properties of the Martian surface

K. E. HERKENHOFF, M. P. GOLOMBEK, E. A. GUINNESS, J. B. JOHNSON, A. KUSACK, L. RICHTER, R. J. SULLIVAN, AND S. GOREVAN

ABSTRACT

The physical properties of rocks and soils on the surface of Mars have been investigated by several landed spacecraft. Studies of these physical properties constrain interpretation of Martian geologic processes and provide engineering data for future mission planning. As on Earth, these properties vary considerably from place to place, and provide constraints on the origin and evolution of the surface materials. Martian soils commonly have thin surface crusts that may be caused by salts cementing grains together. Estimates of soil physical properties at the various landing sites are generally comparable, but rather uncertain in many cases. Rock physical properties, based on abrasion by the Mars Exploration Rover (MER) Rock Abrasion Tool (RAT) and other experiments, vary widely.

20.1 INTRODUCTION

Martian surface rocks and soils record the most recent history of physical and chemical modifications of the surface, perhaps including the effects of climate variations. In some instances, physical properties relate to soil cementation and thereby to diagenesis and chemical deposition. This chapter summarizes the physical and mechanical properties of the Martian surface inferred from landed spacecraft (Viking Landers, Mars Pathfinder, MERs). Knowledge of these surface properties helps to constrain the origin of the surface materials and the processes that have affected them. In addition, information regarding physical and mechanical properties is useful in planning future spacecraft exploration of the surface of Mars.

Soil physical properties of prime interest are grain characteristics, as well as estimates of soil-bearing strength and shear strength. Soil compaction state affects overall strength, and thus (with certain assumptions) derived soil strength allows estimates of other parameters such as bulk density and thermophysical properties. Variations in soil strength can indicate the degree of any postdepositional induration that has occurred. Grain shapes in sedimentary deposits, commonly described in terms of roundness and sphericity, are controlled by mineralogy as well as the type and duration of transport processes. Roundness is a measure of the regularity of the two-dimensional margin of a grain, in terms of the average radius of curvature of all convex sections of the margin (McLane, 1995). Sphericity is the ratio of the diameter of a sphere of the same volume as the particle to the diameter of the smallest circumscribed sphere. The relative abundances of various sizes of grains in a deposit (the degree of sorting) can sometimes be an indicator of grain transport distance. Rock physical properties of interest include hardness and bulk density – properties that generally have been difficult or impractical to evaluate on the Martian surface. Neither magnetic nor electrostatic properties are discussed in this chapter (see, instead, Chapter 16 and Ferguson *et al*., 1999, respectively).

All five successful Mars lander missions returned data that have been used to infer physical properties of the Martian surface: two Viking Landers (1976–82), the Mars Pathfinder lander with Sojourner rover (1997), and two MERs (2004–present). All of these spacecraft carried imaging systems that returned information about natural surfaces and disturbed materials (Huck *et al*., 1975; Smith *et al*., 1997; Moore *et al*., 1999; Bell *et al*., 2003; Herkenhoff *et al*., 2003; Maki *et al*., 2003; Table 20.1). All of these spacecraft also included mechanical devices (wheels, arms, grinding tools) that interacted with soils and rocks, allowing physical properties to be constrained from reactive forces and torques and from the associated responses of the target materials.

Studies of Mars's soil physical properties help to interpret Martian geologic processes and to provide engineering data for future mission planning. The goals of soil physical properties studies are therefore supplementary to the primary objectives of past and planned landed missions, which focus on Mars geology and its evolution, investigating the possibility of life, and finding evidence of water and its effects on the Martian landscape. Instruments for examining the grain size, texture, and mineralogy of rocks and soils have been limited to the surface or near-subsurface, however, thus reducing the ability to characterize soil stratigraphy and rock interiors. Soil scoops/backhoes (Moore *et al*., 1979, 1982) and wheels (Moore *et al*., 1999) allow access to only the nearest subsurface (less than 30 cm; Figures 20.2 and 20.9). Few instruments (all of them on Soviet lunar missions) have been deployed to directly assess soil physical properties like density, soil strength (internal friction and cohesion), and rheology.

Without specialized apparatus designed for measuring soil or rock physical properties, special methods involving adapting available equipment (primarily scoops and wheels) have instead been developed. This approach typically has been complicated by sparse experiment time and data return, low resolution, and complex soil/mechanism

The Martian Surface: Composition, Mineralogy, and Physical Properties, ed. J. F. Bell III. Published by Cambridge University Press.

interface geometry and interactions. For example, the forces required to push a scoop into soil or for a wheel to dig into soil are not directly measured, but are instead estimated from currents drawn by motors during scoop or wheel motions.

Earth-based laboratory tests using Mars soil simulants and flight-identical equipment have been used to "calibrate" the interpretation of experiments conducted on the Martian surface. Soil–machine interaction models that assume homogeneous soils are also used to simulate soil failure and soil properties (Moore *et al*., 1982). Actual Martian soils commonly are more complex and less homogeneous than soil simulants, further complicating interpretation of test results and model calculations (Figures 20.2, 20.7, and 20.9). Remotely sensed data on soil thermal inertia and dielectric properties have also been used to limit the range of possible soil properties like density and the qualitative degree of induration (cementation between soil grains). Data derived using these methods have a high degree of variability, including unrealistic negative cohesion values, and differences of as much as 10° for internal friction angles (ϕ) for similar Mars soils (Table 20.2).

Table 20.1. *Resolution of cameras on Mars landers/rovers*

Camera	IFOV[a] (mrad)	Best resolution[b] (mm)	Comment
Viking Landers	0.7	1.5	High-resolution mode
Mars Pathfinder	1.0	3.0	Before mast deploy
Sojourner	2.9–3.4	2.0	Rectangular pixels
MER Pancam	0.27	1.4	After mast deploy
MER MI	N/A	0.1	At best focus

[a]Instantaneous Field of View; the angular resolution of each pixel.
[b]Size of smallest object that can be recognized (typically 3 pixels across).

20.2 DATA AND INFERENCES

This section describes observations and interpretations of Martian soil and rock strength characteristics, soil grain sizes/shapes, and particle sorting. Implications for the origin and evolution of surface materials are discussed at the end of this section.

20.2.1 Soils

The term "soil" is used here to denote any loose, unconsolidated materials that can be distinguished from rocks, bedrock, or strongly cohesive sediments. No implication of the presence or absence of organic materials or living matter is intended. Martian soils have been observed remotely and *in situ*, and their physical properties can be inferred from analysis of both kinds of data. Remote observations of soil physical properties are summarized elsewhere in this book, for example in Chapters 12, 13, 16, 18, 19, and 21, including analysis of spectrophotometric data acquired by lander instruments. In this section, soil physical properties derived from morphologic and grain size-frequency analyses of Mars landed spacecraft images and from their observed deformation behavior are summarized.

Table 20.2. *Mars soil cohesion (C), internal friction (ϕ), and bulk density (ρ) as inferred from landed missions prior to MER*

C (kPa)	ϕ (°)	ρ (kg m^{-3})	Soil type	Measurement method	Source
−0.34–0.57	31.4–42.2	2000–2200	Cloddy	Wheel dig trenching	MPF Sojourner[a]
0.18–0.53	15.1–33.1	1066–1269	Drift	Wheel dig	MPF Sojourner[a]
1.6 ± 1.2 0–3.7	18 ± 2.4	1150 ± 150	Drift	Scoop trenching and landing pad sinkage	Viking Lander 1[b,c,d]
5.1 ± 2.7 2.2–10.6	30.8 ± 2.4	1600 ± 400	Blocky	"	Viking Lander 1[b,c,d]
1000–10 000	40–60	2600	Rocks	"	Viking Lander 1 and 2[b,c,d]
1.1 ± 0.8 0–3.2	34.5 ± 4.7	1400 ± 200	Crusty to cloddy	"	Viking Lander 2[b,c,d]
2.7–3.4	22.0–27.0		Lunar intercrater terrain	Vane shear tester	Lunokhod 1 and 2[e]

[a]Moore *et al*. (1999).
[b]Moore *et al*. (1982).
[c]Moore *et al*. (1987).
[d]Moore and Jakosky (1989).
[e]Kemurdzhian *et al*. (1978).
Note that Viking-based rock properties actually were unmeasured; these were simply broad estimates based on assumed similitude with many terrestrial silicate rocks. Lunar regolith properties along Lunokhod rover traverses are shown for comparison.

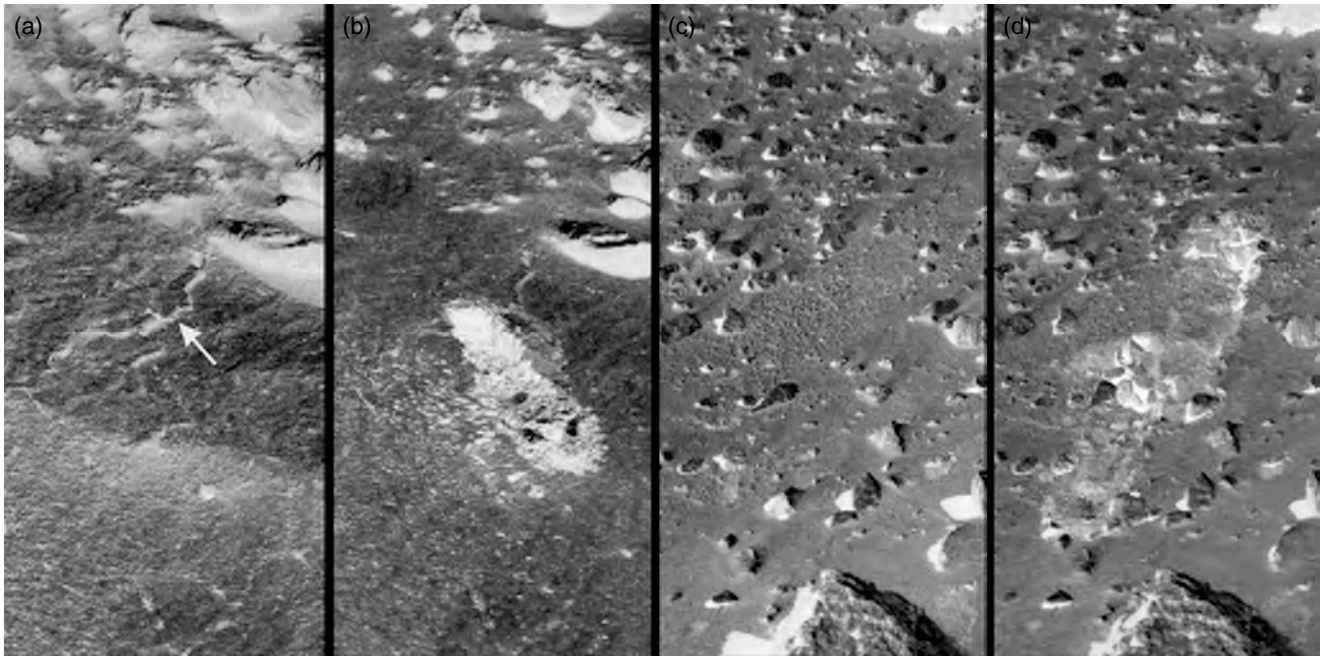

Figure 20.1. Example Viking Lander 1 images of the drift and blocky material soil classes, shown for the natural surfaces and after trenching into the materials. (a) Natural surface of drift material from Sandy Flats at VL1 is exposed from near the center to bottom of the frame (Viking Lander Image ID: 11A055/008). The sinuous pattern at the surface (indicated by arrow) could be an expression of cross laminations in the subsurface. (b) Same area of drift material is shown after trenching during sample acquisition (Image ID: 11A058/008). The trench exhibits steep walls, along with a domed and fractured surface surrounding the far end of the trench. The trench is about 8 cm wide, 45 cm long, and 5 cm deep. (c) At the center of the frame is an area of blocky material at VL1 known as Rocky Flats, which shows a characteristic pebbly texture (Image ID: 12A140/024). (d) Trenches into the Rocky Flats area are seen after several sample collection activities (Image ID: 12B163/073). The disrupted areas at the far ends of the trenches clearly show the blocky nature of this material. Multiple trenching sequences excavated down to a maximum depth of about 5 cm. The upper trench is about 9 cm wide.

Viking Landers

Physical properties investigations were conducted by the two identical Viking Lander spacecraft that operated on the surface of Mars for several Earth years between 1976 and 1982. The Viking Lander 1 (VL1) landing site is located in Chryse Planitia on a surface that includes drifts superimposed on a rocky substrate (Binder *et al*., 1977; Arvidson *et al*., 1989; see also Chapter 21). Viking Lander 2 (VL2) landed on the opposite side of Mars in Utopia Planitia. The VL2 site is characterized by lower relief, but is littered with centimeter- to meter-sized rocks perched on the surface and partially buried in soil (Mutch *et al*., 1977; see also Chapter 21). The objectives of the Viking physical properties investigation were to determine soil-bearing strengths, cohesions, angles of internal friction, porosities, thermal properties, grain sizes, and adhesions (Moore *et al*., 1987). However, there were no Viking Lander instruments designed to directly measure any of these parameters. Instead, information on material physical properties was derived from imaging observations of the interactions between surface materials and spacecraft components, such as footpad penetration and erosion by descent rocket exhaust during landing. In addition, the behavior of materials was interpreted from electro-mechanical resistances during surface sampler arm activities while collecting samples, trenching, sieving, and pushing rocks. Moore *et al*. (1987) provide a detailed description of the surface sampler system used in many of the physical properties experiments. Moore *et al*. (1987) also give a complete catalog of the types of experiments done and a chronology of the lander activities associated with the physical properties investigations.

The surface sampler arm on each Viking Lander consisted of an extendable boom that pivoted in both azimuth and elevation. At the end of the surface sampler arm was a collector head that had a fixed lower jaw with a backhoe underneath and a movable upper jaw that had a grating with 2 mm holes for sieving. Sieving was done by inverting the collector head and vibrating. Motor currents from the arm were recorded during sample collection to provide additional data on surface material properties. The area accessible to the surface sampler arm was located in front of each lander and was referred to as the sample field, which comprised an annular area about 1.5 m across. Analyses of physical properties experiments produced a classification of sample field materials at the two sites that included three types of soil-like materials, and rocks. The soil materials listed in order of increasing strength are drift material, crusty to cloddy material, and blocky material (Moore *et al*., 1977, 1987).

Drift material, which is found only at the VL1 site, is the weakest of the soil materials studied by Viking. It covers about 14% of the sample field (Moore and Jakosky, 1989). Its name derives from several locations outside the sample field where this material is seen in drift forms that cover areas from 1 to 10 m across. Some of the drifts in the midfield are eroded and expose crosslaminations. Closer to the VL1, drift material appears smooth, suggesting unresolved, very fine-grained silt to clay-size particles (Figures 20.1a and b).

During the VL1 landing, footpad number 2 penetrated 16.5 cm into drift material and became partially buried. Experiments known as "backhoe touchdowns" were conducted to help determine the cohesion of the material. In a backhoe touchdown experiment, the collector head was positioned over a target with the backhoe pointing down toward the surface. The arm was then lowered onto the surface. As the backhoe penetrated into the surface material, the collector head would rotate about 10° until a contact switch stopped the arm motion. Backhoe touchdown sequences into drift material generated penetration depths of 3–4 cm (Moore *et al.*, 1987).

Excavation of a deep hole into an area of drift material known as Sandy Flats was accomplished by pushing the backhoe into the surface and retracting the arm. The deep hole trench sequence at Sandy Flats retracted the backhoe 48 times and produced a trench that was 23 cm deep with average wall slopes of 68°. By the end of the mission, these trench walls had remained unchanged for over 1000 sols (Moore *et al.*, 1987). Drift material has the lowest angle of friction (18°) among the three soil materials based on analyses of trenches. The slope stability of trench walls suggests low cohesion (less than 3.7 kPa with an average of 1.6 kPa; Moore *et al.*, 1982, 1987) for drift material. These cohesion values are smaller than most dry, fine-grained terrestrial sediments. Drift material appears to have the consistency of loose baking flour (Arvidson *et al.*, 1989). The bulk density of the drift material was estimated from X-ray Fluorescence Spectrometer (XRFS) data to be $1150 \pm 150\ \mathrm{kg\,m^{-3}}$ (Clark *et al.*, 1977). Thus, drift material is also likely to be porous, given its low bulk density.

Crusty to cloddy material covers about 86% of the VL2 sample field, occurring between individual rocks (Moore and Jakosky, 1989). Crusty to cloddy material is characterized by relatively smooth and fractured surfaces (Figure 20.2a). It also tends to break up into small 0.5–1 cm sized clods. Crusty to cloddy material occurs at or near the surface and appears to be underlain by less cohesive material (Moore *et al.*, 1982). Disrupted areas of crusty to cloddy material around trenches tend to have broken, platy slabs of crust (Figure 20.2b). A deep trenching sequence using 47 backhoe retractions reached a depth of 11–12 cm into crusty to cloddy material. In addition, backhoe touchdown experiments into the surface of crusty to cloddy material produced penetration depths of only about 0.9–1.4 cm (Moore *et al.*, 1979). These observations suggest that crusty to cloddy material is stronger than drift material based on shallower trenches and backhoe penetrations. However, numerous sieving operations with the collector head easily disaggregated clods of this material, with the loose particles passing through the 2 mm holes in the sieve. Deformations around the edges of trenches and the stability of trench walls suggest that crusty to cloddy material has an angle of internal friction of around 35° and cohesions <3.2 kPa, with an average of 1.1 kPa (Moore *et al.*, 1982) – still low when compared to dry, fine-grained terrestrial soils. Several failed attempts to collect rock fragments from areas of crusty to cloddy material suggest that millimeter- to centimeter-size rock fragments or strong clods do not commonly occur within this material (Moore *et al.*, 1987). Overall, the observations suggest that the crusty to cloddy material consists of fine-grained material that is weakly cemented together by salts (Clark *et al.*, 1982; Arvidson *et al.*, 1989).

Figure 20.2 Example Viking Lander 2 images of the crusty to cloddy soil class, shown before and after trenching into the materials. (a) A region of crusty to cloddy material from VL2 is shown before any disturbance by trenching (Image ID: 22A007/001). Note the relatively smooth crusty area cut by fractures located near the center of the image and indicated with the arrow labeled 1. The rock labeled with arrow 2 is about 25 cm across. (b) The same area is seen after two sample acquisitions produced a trench into the crusty material (Image ID: 22A247/030). Trenching disrupted the surface to form plates of crusty material several centimeters across and about 1 cm thick. The first sample acquisition reached a depth of about 2–3 cm, whereas the second one excavated down to about 4–5 cm. The overall length of the trench is about 29 cm.

The blocky material found at the VL1 site is the strongest of the soil materials at the two Viking lander sites. Blocky material occurs between rocks and drift material at the VL1 site, and covers about 78% of the VL1 sample field (Moore and Jakosky, 1989). Blocky material is characterized by centimeter-sized prismatic clods (Figure 20.1c). When disrupted by trenching, it forms 2–4 cm sized fragments (Figure 20.1d). The descent engines eroded into the blocky material during landing to expose a fractured material that appears to be cohesive or indurated. Footpad number 3 of the VL1 landed on top of blocky material and only penetrated 3.6 cm, as opposed to the 16.5 cm of penetration of footpad 2 into nearby drift material. Similarly, backhoe penetration depths into blocky material of 0.5–1.4 cm were less than that for drift material (Moore *et al.*, 1987). Trenching using 48 backhoe retractions to dig into the surface excavated to a depth of about 13 cm into blocky material (Moore *et al.*, 1979) and required large forces by the surface sampler arm (Moore *et al.*, 1982). Sieving and purging sequences while collecting samples of blocky material yielded millimeter- to centimeter-sized rock fragments or strong clods. Analyses of trenches dug into blocky material suggest an angle of internal friction of 31° and cohesions

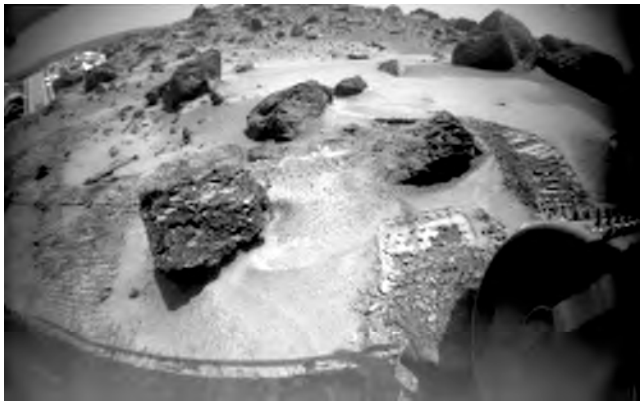

Figure 20.3. Sojourner rover camera image of wheel tracks showing bright reflective molds of cleats, flakes of compressed drift deposits, and darker, less-well-sorted underlying soil deposits.

between 2.2 and 10.6 kPa, with an average of 5.5 kPa (Moore *et al*., 1982). The measurements got from XRFS show that these coarse clods are enriched in S and Cl (Clark *et al*., 1982), which suggests that the cohesion of blocky material is related to cementation by salts (Moore and Jakosky, 1989).

Sojourner/Mars Pathfinder

The Sojourner rover, carried aboard the Mars Pathfinder lander, was the first successful wheeled vehicle to interact with the Martian surface, allowing soil physical properties to be studied at multiple locations at the landing site near the mouth of the Ares Vallis catastrophic outflow channel. Pathfinder lander airbag bounce and retraction marks also provided information on disturbed surface materials before the rover was deployed. Airbag bounce and retraction marks appear darker than undisturbed soil, suggesting the presence of a thin, bright surface layer. Airbag retraction marks are shallow trenches radial from the lander, with pebbles and rocks entrained in the nearby soil (Golombek *et al*., 1999a). Rover tracks also generally appear dark except in locations where the bright surface material is compressed into smooth, reflective bright clods that carry imprints of the rover wheel cleats (Figure 20.3; Moore *et al*., 1999). The bright surface material is the same color as the dust in the atmosphere (light yellowish brown), and drift material at least on the surface of wind tails behind rocks and within the wheel tracks appears to be very fine-grained, porous, and compressible. These observations argue that this material is micron-sized dust that has settled from the atmosphere. Beneath the bright, fine-grained drift is darker, poorly sorted soil composed of unresolved fine-grained material mixed with pebbles, cobbles, and rock fragments. This cloddy soil is similar to moderately dense soils on Earth.

More diagnostic in understanding the mechanical properties of the soil than simply imaging the wheel tracks were the 14 special soil mechanics tests performed by the Sojourner rover over its ~100 m traverse. These tests were performed by locking 5 wheels and rotating the 6th wheel in quarter-revolution steps while measuring the rocker bogie differential angle (wheel depth with time) and the motor current, which was converted to wheel torque (during revolutions

Figure 20.4. IMP image of Sojourner rover performing APXS measurement of "Scooby Doo," a hard, indurated, soil-like deposit whose elemental composition is similar to other soils but which was not noticeably scratched or marked during "road warrior" rock wheel scratch tests.

and no-load "wheelies") and shear and tractive forces using the results of a series of tests on a variety of soil types on Earth. Derived normal and shear stresses were used to iteratively solve a standard Mohr Coulomb failure criterion that included cohesion and friction angle (angle of internal friction) or coefficient of friction. The angle of internal friction was estimated from the angle of repose of excavated piles of material that had low cohesion (Moore *et al*., 1999). Estimates of the angle of internal friction are believed to be better constrained than cohesion (which is very small) by the experiments. The abrasiveness of the Martian dust was measured from the wear on a thin metal film mounted on one of the rover wheels (Ferguson *et al*., 1999).

Results of the Sojourner soil mechanics experiments are consistent with soil simulants tested on Earth and suggest that cloddy soil behaves like moderately dense soils on Earth, with friction angles near 34°–39°, low cohesion of 0.0–0.42 kPa, and angle of repose of 33°–38° (Moore *et al*., 1999). Scooby Doo, a bright patch of cohesive soil or rock that had a chemical composition similar to other soils, was undeformed by the rover wheel cleats during a scratch test, indicating that it was well-indurated, resembling hardpan on Earth (Figure 20.4). Mechanically, cloddy soils at the Pathfinder site resemble the crusty to cloddy soils at VL2, albeit with lower cohesion. Scooby Doo resembles blocky material at VL1, and the drift deposits at the Pathfinder site are like very porous and weak drift deposits at VL1. Inferred bulk densities of cloddy soils estimated from their friction angles (Moore *et al*., 1999), assuming they behave like lunar soil simulants (Mitchell *et al*., 1972), are 1285–1518 kg m^{-3} for average friction angles of 34°–37°; higher bulk densities of 2000–2200 are likely for well-indurated materials such as Scooby Doo at Pathfinder and blocky soils at VL1. These

Figure 20.5. Sojourner rover wheel tracks in "Cabbage Patch" showing cloddy deposits and at least one rounded pebble.

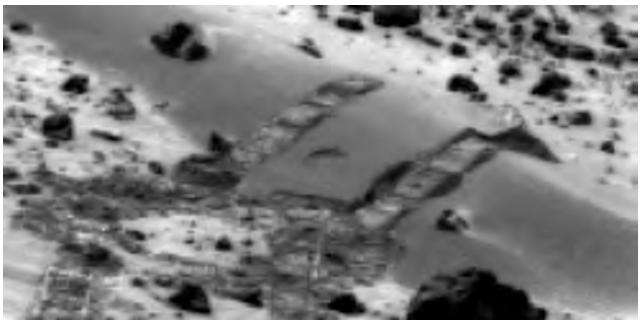

Figure 20.6. IMP image of "Mermaid" duneform showing reflective rover tracks, darker subsurface soils, pile of material excavated by a rover wheel, and circular spot where APXS disturbed soil during measurement. Pile of material allowed measurement of angle of repose, and close-up rover images show the dark, poorly sorted substrate.

bulk densities are also similar to those estimated from the radar reflectivity of the surface (Golombek *et al.*, 1999b; see also Chapter 21) via extrapolation of a radar echo model (Hagfors, 1964; Evans and Hagfors, 1968) and a relation between bulk density and normal reflectivity (Olhoeft and Strangway, 1975). Cloddy soils at the Pathfinder site, many of which contain pebbles (Figure 20.5), may be poorly sorted fluvial materials deposited by the Ares and Tiu catastrophic floods (Golombek *et al.*, 1999a; Moore *et al.*, 1999); the finer fractions may have been reworked via eolian activity (Greeley *et al.*, 1999, 2000). Drift deposits may be dust deposited from atmospheric suspension, and in the case of bright dust covering at least the surface of wind tails, may be sculpted by the wind (Moore *et al.*, 1999). Sojourner tracks in the "Mermaid" duneform appear bright, suggesting a significant fraction of fine-grained (dusty) material there (Figure 20.6). Comparison of wear results of thin metal films shows that the Martian dust is comparable to fine-grained soils of limited hardness (Ferguson *et al.*, 1999).

Mars Exploration Rovers

As of early 2007, the two MERs *Spirit* and *Opportunity* have each traversed distances of more than 6 and 10 km at their respective landing sites in more than three years of surface operations. Each rover carries an identical science payload of remote-sensing and arm-mounted, surface-contact instruments. Both MER vehicles performed the following investigations related to physical properties (Arvidson *et al.*, 2003): (i) quantification of dust accumulation and dispersal dynamics by periodically monitoring the rover decks with the Pancam (Bell *et al.*, 2003) and Miniature Thermal Emission Spectrometer (Mini-TES) (Christensen *et al.*, 2003); (ii) inference of soil properties from analyses of wheel track patterns, wheel sinkage, and wheel slippage during traverses; (iii) extraction of along-track terrain topography and physical properties from rover wheel and suspension telemetry recorded during traverses; (iv) excavation of trenches using rover wheels to characterize mechanical properties of soils with depth; (v) analysis of rock grind telemetry from the RAT (Gorevan *et al.*, 2003) to infer rock strength; and (vi) observations of the Mössbauer Spectrometer (Klingelhöfer *et al.*, 2003) and Microscopic Imager (MI) (Herkenhoff *et al.*, 2003) contact sensor interactions with surface materials. Initial results of the MER physical properties investigations covering the primary missions of both rovers were reported by Arvidson *et al.* (2004a,b).

The ring-shaped Mössbauer contact plate applied a force of ~1 N (1 N is about the weight of a 102 g apple in Earth's gravity, or 0.225 lb) to soils at both landing sites to refine knowledge of instrument arm positioning relative to a surface target and/or to specifically observe the effect of slight pressure applied to the soil. MI images of Mössbauer contact plate soil impressions show that the natural texture of fine-grained soils typically is obliterated on contact (Figures 20.7 and 20.8). The observed molding behavior under pressure, exhibited by most soils at both MER sites, suggests that some soils include weak particles that are easily crushed, and/or a significant fraction of unresolved very fine particles is present that reconfigures among voids between larger particles under applied pressure.

Soils at the Gusev site generally are covered by a layer of dust typically less than 1 mm thick that was easily disturbed by *Spirit*'s landing system and wheels (see also Chapter 13). Darker soils beneath this surface layer commonly showed evidence of cohesion when disturbed by the rover wheels or lander airbags. A weak surface crust a few millimeters thick (including the dust layer) was easily crushed by the rover wheels or Mössbauer contact plate. MI images of crushed soils show that fine grains are molded to form casts that are smooth at sub-millimeter scales, implying a significant fraction of fine-grained material (Figure 20.9). Some of the fine particles may be agglomerates of dust grains that are held together by electrostatic cohesion or minor cementation (Herkenhoff *et al.*, 2004a).

The aeolian bedform dubbed "Serpent" was disturbed by *Spirit*'s wheels, exposing weakly cohesive, fine-grained material beneath a surface layer of very coarse sand and granules (Figure 20.10). Larger wheel trenches dug into other soils on the plains between the lander and the Columbia Hills all retained wall slopes greater than typical angles of repose. They also yielded break-away clods from the walls, indicating that some minor cohesion is pervasive with depth, although it must be even weaker than that of the

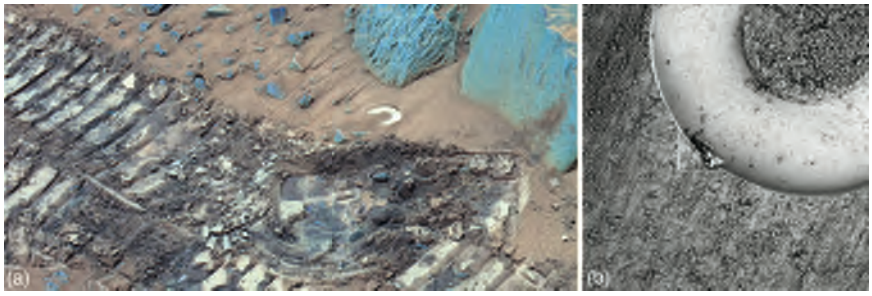

Figure 20.7. (a) *Spirit* Pancam false-color view of tracks and Mössbauer imprint into dusty aeolian drift material, obtained near the summit of Husband Hill on Sol 589. Pancam filters are L2 (753 nm), L5 (535 nm), and L7 (432 nm) stretched into red, green, and blue, respectively. The Mössbauer imprint is the bright, partial ring feature at central upper-right in this view. (b) *Spirit* MI image of the same Mössbauer contact plate imprint, obtained on Sol 588 in full shadow. The MI was rotated at the time of imaging relative to the orientation of (a). MI view is ~31 mm across. (For a color version of this figure, please refer to the color plate section or to the e-Book version of this chapter.)

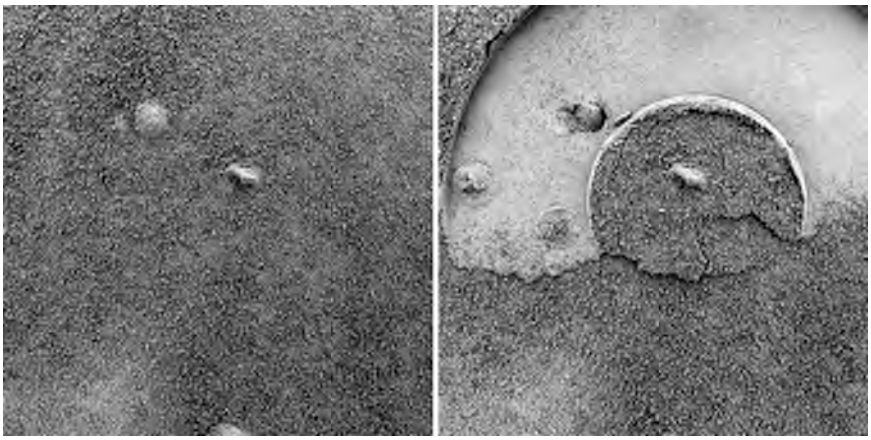

Figure 20.8. *Opportunity* MI images of a relatively rare (at Meridiani Planum) bright, dusty soil before (left) and after Mössbauer contact. Dust-sized particles (seen clumped into resolved agglomerates) allow the soil to accurately mold the Mössbauer contact plate, including screw heads on the left. Fissures near the center indicate small amounts of surface cohesion. Images 1M133421996IFF0830P2957M2F1 and 1M133598234IFF0830P2957M2F1 were obtained on Sols 59 and 61, respectively. Both views are about 31 mm across. Compare this pair of images with Figure 20.9 (Gusev).

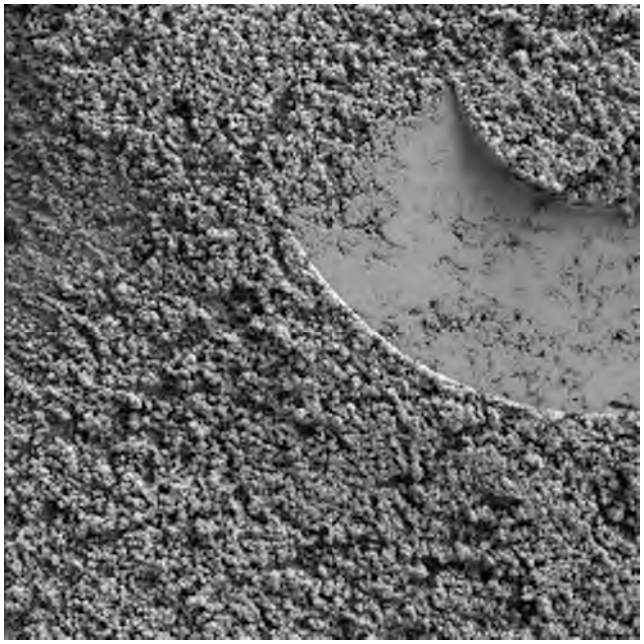

Figure 20.9. *Spirit* MI image 2M147677362IFF8800P2976M2F1 of a Mössbauer plate impression into dusty soil. Unresolved dust particles apparently have clumped together into irregularly shaped, resolved agglomerates that are easily crushed and molded by the ~1 N contact force. The image, spanning about 31 mm, was obtained on Sol 240 when the target was fully shadowed by the instrument, with diffuse illumination from top.

fragile ~1 mm surface crust (Figure 20.11). Trenching depths achieved varied between ~6 and 10 cm. A soil crust on the flank of Husband Hill showed evidence for cementation of well-sorted sand grains (Figure 20.12). Visual measurements of wheel rut depths in various soils (Figure 20.13) yielded preliminary estimates of bearing strength from about 15 to 130 kPa, cohesive strength of ~1–7 kPa, and angle of internal friction of ~20°–25°, using semi-empirical wheel–soil interaction theory calibrated to the shape of the MER wheel (Richter *et al*., 2006).

The upper ~1 mm of soil at Meridiani Planum also commonly appears to be weakly cohesive in MI images of soil disturbed by the Mössbauer contact plate or rover wheels (Figure 20.14; Herkenhoff *et al*., 2004b). The cohesion may be due to the presence of chloride and/or sulfate salts, a conclusion that is consistent with Alpha Particle X-Ray Spectrometer (APXS) observations of soils at the *Opportunity* landing site (Rieder *et al*., 2004). These salts may have precipitated from thin films of water that formed during warmer periods and that dissolved salts in dust particles. In places, the cohesion appears to be minor and easily destroyed (Figure 20.15). The Meridiani soil surfaces typically have a bimodal size distribution, with very coarse sand grains and granules up to 6 mm in diameter, along with very fine (<125 microns) dark sand (Soderblom *et al*., 2004; Weitz *et al*., 2006; see also Chapter 13). Trenches dug into soils by *Opportunity*'s wheels showed that the coarser grains are concentrated at the surface, likely by aeolian removal of the finer particles (Figure 20.16), forming a lag that

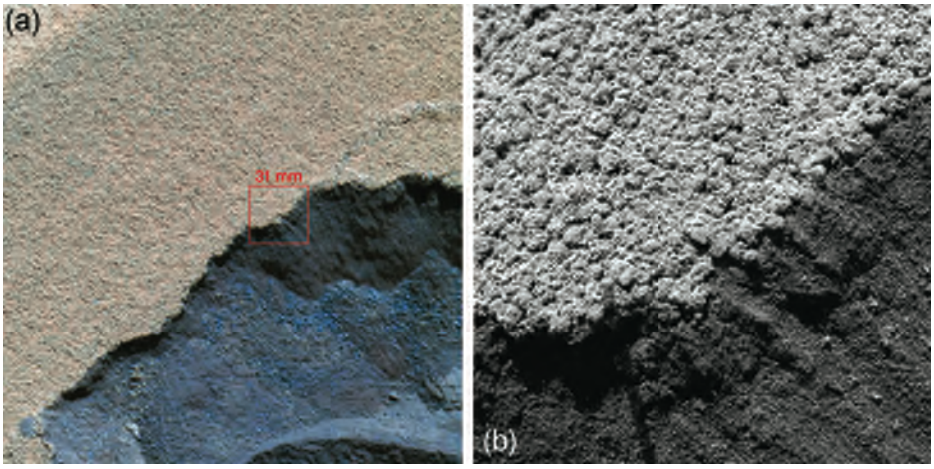

Figure 20.10. (a) *Spirit* Pancam false-color view of the wheel scuff performed on Sol 72 into "Serpent," an aeolian bedform near the rim of Bonneville crater on the plains west of the Columbia Hills. Pancam filters are L2 (753 nm), L5 (535 nm), and L7 (432 nm) stretched into red, green, and blue, respectively. The brighter, redder, dusty exterior contrasts with the darker interior of the feature. Red square shows MI location. (b) MI image 2M132842058IFF2000P2977M2F1 of the edge of the wheel scuff, obtained on Sol 73. A very thin, relatively bright dust layer covers a monolayer of rounded, very coarse sand, which overlies an ~8 mm weakly cohesive layer dominated by finer grains, with similarly fine materials further below (lower right of image). View is about 31 mm across, illuminated from top. (For a color version of this figure, please refer to the color plate section or to the e-Book version of this chapter.)

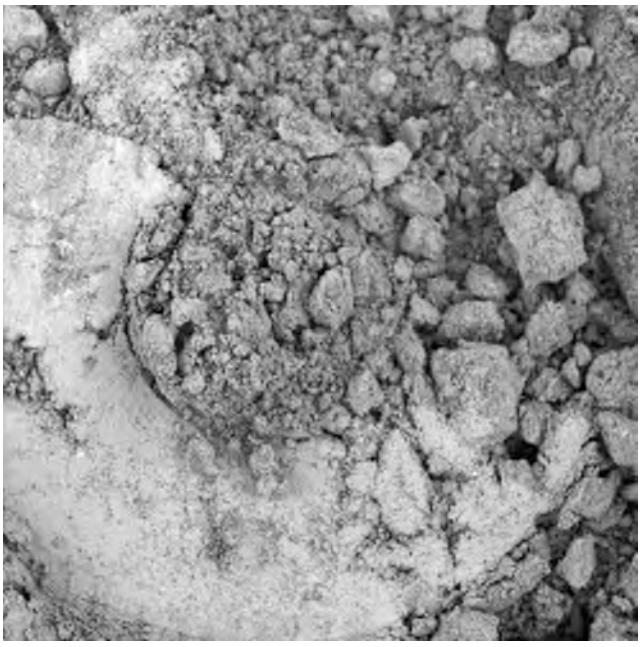

Figure 20.11. *Spirit* MI image 2M136501952IFF37CAP2957M2F1 of a Mössbauer imprint into debris on the floor of the Sol 113 wheel trench. Soil clods are easily compressed and molded by the ~1 N contact force of the contact plate, implying relatively weak cohesion. The image spans about 31 mm and was obtained on Sol 114 when the target was fully shadowed by the instrument.

protects finer grains in the subsurface from further erosion (Arvidson *et al.*, 2004b; Soderblom *et al.*, 2004; Sullivan *et al.*, 2005; Jerolmack *et al.*, 2006; Weitz *et al.*, 2006). Trench walls steeper than the angle of repose and the presence of break-away clods from the walls are additional evidence for soil cohesion extending to maximum trench depths of about 10 cm. Wheel tracks, Mössbauer contact plate impressions, and airbag bounce marks showed that the soil can be finely molded, indicating the presence of a substantial fraction of very fine particles, unresolved by the MI, that fill voids during compression and remolding. Soil physical properties estimated from wheel rut depths exhibited similar values as those inferred for the Gusev site (Arvidson *et al.*, 2004a,b).

Figure 20.12. *Spirit* MI image of a disrupted soil crust containing well-sorted 200–300 μm grains, overlying finer material (darker zones in image). Weak soil crusts of varying thicknesses and strengths are common at both MER landing sites. Image 2M170218789IFFAAEEP2976M2F1, obtained on Sol 494 with direct illumination from the upper left, spans about 31 mm.

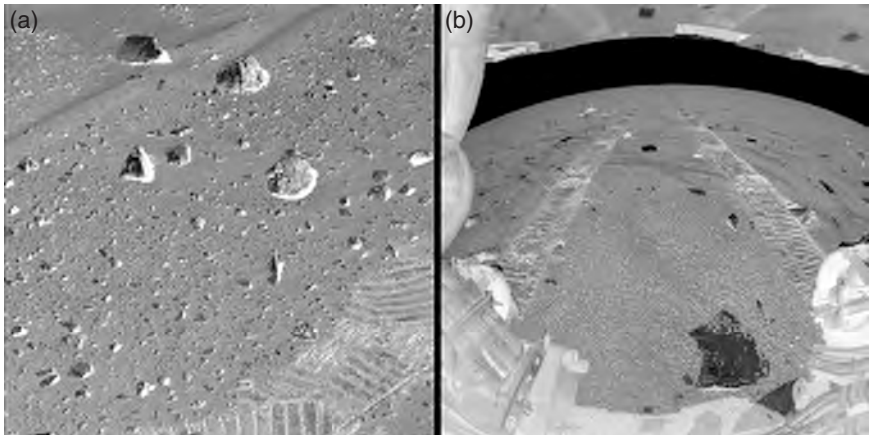

Figure 20.13. Examples of MER wheel tracks. (a) *Spirit* Pancam R1 (436 nm) frame 2P129996790RAD0506P2599R1C4 (Sol 41), showing wheel track with comparatively small rut depth on plains surface between the landing site and Bonneville crater. (b) *Opportunity* Rear Hazcam frame 1R135651546 (Sol 84), showing wheel tracks with comparatively large rut depth on Meridiani plains surface close to Fram crater.

Figure 20.14. *Opportunity* MI image 1M173457602IFF55W4P29-36M2F1 obtained where *Opportunity* became severely bogged (embedded) while climbing an unusually large ripple, informally dubbed "Purgatory." This view, about 31 mm across, shows part of a tablet of soil compacted and remolded by the wheel cleats, then deposited alongside a track. Hematitic spherules (interpreted as concretions) 1–2 mm in diameter have been incorporated into this wheel-made, molded clod. They were mixed with and embedded within a finer, poorly sorted soil matrix that acquired slightly cohesive properties when compacted by the wheel. After creation, the tablet was subjected to aeolian erosion of the matrix, exposing the 1–2 mm concretions, particularly along the tablet's lower edge (note pedestals). During *Opportunity*'s ~40 sol stay in this area, wind events were seen to affect only areas disturbed by the rover, such as this example viewed on Sol 510.

Soil thermal inertia was derived using the relations proposed by Presley and Christensen (1997), which link bulk thermal conductivity of soils at Martian atmospheric pressure to soil bulk density, with the density estimated from wheel rut depth analysis. The resultant estimates range between 130 and 150 $J\,m^{-2}\,K^{-1}\,s^{-1/2}$ and are lower bounds because the effect of soil cohesion on the thermal inertia is not included in the Presley and Christensen model.

Discussion

The mechanical properties of soils at the landing sites are consistent with inferences made from orbital thermal inertia measurements (see Chapters 9, 18, and 21). Thermal inertia is a measure of the resistance of surface materials to a change in temperature that can be related to particle size, bulk density, and cohesion (Kieffer *et al.*, 1977; Christensen and Moore, 1992). The fine component thermal inertia is the thermal inertia of the soil after the thermal radiance of the rocky component has been factored out (Kieffer *et al.*, 1977; Christensen, 1986). Because rocks consist of <20% of the surface of the landing sites, their effect on the bulk inertia can be factored out via simple models of the effective thermal inertia of the rock population based on their diameter (Golombek *et al.*, 1999b, 2003). For the bulk thermal inertia of the Pathfinder site of 435 $J\,m^{-2}\,K^{-1}\,s^{-1/2}$ and the estimated effective inertia of the measured rock size-frequency distribution of 1700 $J\,m^{-2}\,K^{-1}\,s^{-1/2}$, a fine component thermal inertia of about 320 $J\,m^{-2}\,K^{-1}\,s^{-1/2}$ was derived (Golombek *et al.*, 2003), which is consistent with that expected for the observed poorly sorted, moderately dense, cloddy soils (Moore *et al.*, 1999). Lower fine component thermal inertias at VL1 (240 $J\,m^{-2}\,K^{-1}\,s^{-1/2}$) and VL2 (170 $J\,m^{-2}\,K^{-1}\,s^{-1/2}$) derived in a similar way (Golombek *et al.*, 2003) are consistent with the greater drift coverage at VL1 (18%–30%) and at VL2 (40%) (Moore *et al.*, 1999). The fine component thermal inertia derived from rock abundance counts along *Spirit*'s traverse from the landing site to the rim of Bonneville crater similarly varies from 240 to 140 $J\,m^{-2}\,K^{-1}\,s^{-1/2}$ and can be related to the increased coverage of very-low-thermal-inertia dust (Golombek *et al.*, 2005). In the case of Meridiani Planum, the bulk and fine component thermal inertia are effectively the same due to the lack of rocks, and the orbital thermal inertia of 200 $J\,m^{-2}\,K^{-1}\,s^{-1/2}$ corresponds directly to that expected (Presley and Christensen, 1997) from a surface dominated by the ubiquitous 0.2 mm fine sand observed by the rover (Herkenhoff *et al.*, 2004b).

Estimates of the thermal inertia based on MER Mini-TES observations and soil physical properties (including cohesion) are presented in Chapter 21. The Mini-TES results, corrected for observed rock and clast abundances (Fergason *et al.*, 2006) (150–200 $J\,m^{-2}\,K^{-1}\,s^{-1/2}$ for Gusev soils and 100–150 $J\,m^{-2}\,K^{-1}\,s^{-1/2}$ for Meridiani Planum soils), are

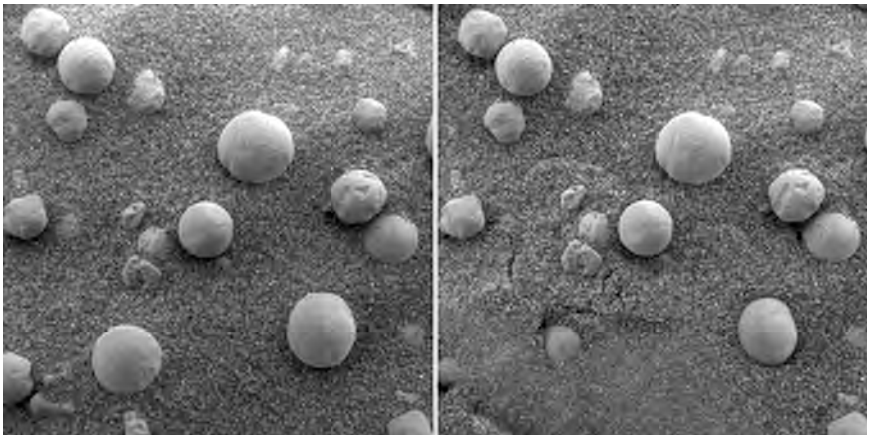

Figure 20.15. *Opportunity* MI images of hematitic concretions and mafic sand in Eagle crater, before (left) and after (right) being touched with the ring-shaped Mössbauer contact plate. Minor fissures opening in slightly distorted soil (right) indicate slight original cohesion. This cohesion is destroyed where more aggressive distortion occurs under the contact plate itself, resulting in self-burial of one of the larger concretions by effectively cohesionless sand. MI images 1M129426966IFF0300P2932M1F1 and 1M129430301IFF0300P2932M1F1 were obtained on Sol 14 in the shadow of the instrument, with diffuse illumination from the top. Each image is about 31 mm across.

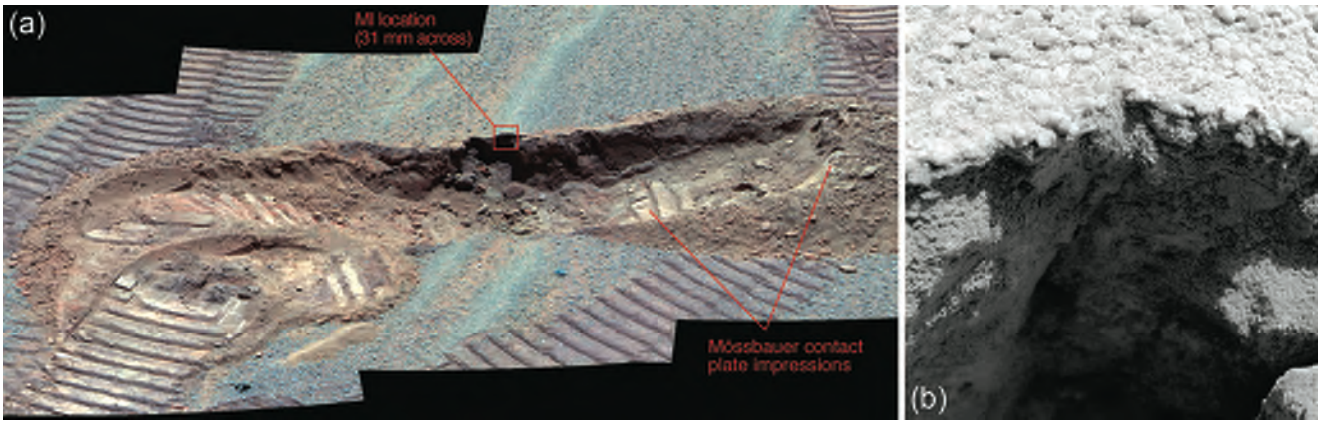

Figure 20.16. (a) *Opportunity* Pancam false-color view of a wheel trench dug on Sol 73 in the Anatolia area on the Meridiani plains between Eagle and Endurance craters. Pancam filters are L2 (753 nm), L5 (535 nm), and L7 (432 nm) stretched into red, green, and blue, respectively. In this view, hematite-enriched spherules several millimeters in diameter are blue, and are scattered across the undisturbed areas between ripples. Low ripples are coated with much smaller ~1 mm rounded hematite grains (also blue, not individually resolved by Pancam). The wheel trench bisected the (blue) ripple extending down the center of this view. The shadowed area on the trench far wall, where the ripple is bisected, is a collapse "cavern" that formed late in the trenching process (as seen in front Hazcam images obtained periodically during trenching), shedding break-away cohesive clods to the base of the trench wall. Maximum trench depth is about 10 cm. Red inset shows MI view location. (b) MI image 1M135284929IFF10CGP2956M2F1 of the rim of the trench. The ripple crest is seen in cross section in the upper middle of this view, where a surface of ~1 mm rounded hematite-enriched spherules form a thin lag. The ripple interior is dominated by ~100 μm sand and even finer, unresolved grains. View is about 31 mm across, illumination from upper right. (For a color version of this figure, please refer to the color plate section or to the e-Book version of this chapter.)

similar to the fine-component thermal inertias derived from TES and THEMIS data (140–200 $J\,m^{-2}\,K^{-1}\,s^{-1/2}$) (Golombek *et al.*, 2005).

Minimum thermal inertias inferred from MER wheel rut depth analysis (~130–150 $J\,m^{-2}\,K^{-1}\,s^{-1/2}$) are somewhat lower than those obtained from orbital observations. This may be explained by the presence of cements interspersed in the soils that would enhance thermal conductivity (and thus thermal inertia) over that predicted by the empirical relation of Presley and Christensen (1997), which assumes loose, noncemented particulate materials. MER APXS and Viking Lander XRFS data are consistent with the presence of such ubiquitous, dispersed cements in the form of sulfates (Clark *et al.*, 1982; Wänke *et al.*, 2001; Rieder *et al.*, 2004).

From a strength perspective, MER soils most resemble the VL1 "blocky" soil type, although larger soil deformations by the wheels and Mössbauer spectrometer contact plate in some places suggest locally weaker deposits. Preliminary cohesion estimates obtained from the MER wheel rut depth analyses (Arvidson *et al.*, 2004a,b) are similar to results of Viking Lander sample trench analyses but higher than those derived from the Pathfinder Sojourner soil mechanics investigations (although large uncertainties were assigned to the Pathfinder soil cohesion retrievals by the investigators themselves) (Moore *et al.*, 1999).

Several empirical relations have been proposed between the shear strength of soils and their bulk density, such as those of Mitchell *et al.* (1972) which relate soil void ratio to internal friction angle and to cohesion respectively, assuming that the material physically behaves like lunar regolith. For a mineral density of 2900 $kg\,m^{-3}$ (the range of mineral densities in the lunar soil is 2300–3200 $kg\,m^{-3}$ [Carrier *et al.*, 1991]), these relations were applied to the inferred MER soil strengths to produce corresponding estimates for bulk density, which was found to range from ~1200 to ~1400 $kg\,m^{-3}$. A simpler approach, perhaps justified by

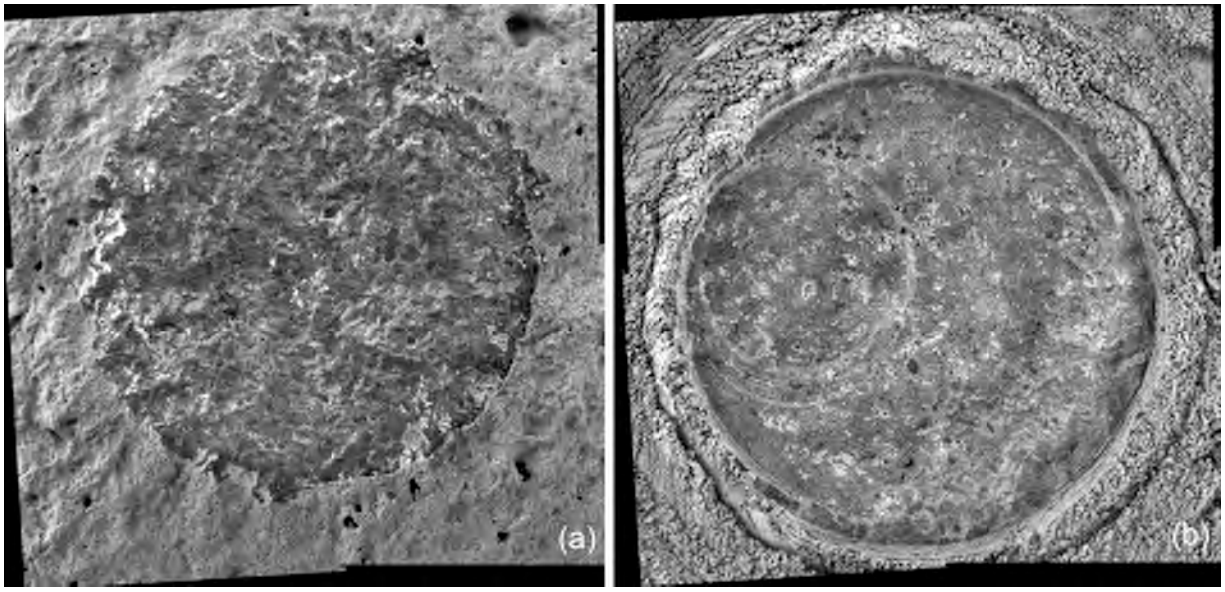

Figure 20.17. *Spirit* MI mosaics of target "Chisel" on rock "Wishstone" before ((a) acquired on Sol 333) and after ((b) acquired on Sol 334) RAT grinding. Each mosaic is about 5 cm across; all images taken while target was fully shadowed.

observed lateral and depth-dependent soil heterogeneities (e.g., coarse particle lags and slightly cohesive soil crusts), involves assuming a typical porosity of around 50% applied to a mineral density of 2700–2900 kg m^{-3} yielding a similar range of bulk densities. These bulk densities are similar to those inferred from measured radar reflectivities of Gusev and Meridiani of 1200 kg m^{-3} (Gusev) and 1500 kg m^{-3} (Meridiani) (Golombek *et al.*, 2003). Elevated radar reflectivities of 0.05 across Meridiani Planum may be caused partly by the observed lag deposit of hematite-rich spherules.

20.2.2 Rocks

Rocks are abundant at both Viking Lander sites. Rocks larger than 3.5 cm cover about 8% of the sample field at the VL1 site and about 16% at the VL2 site (Moore and Jakosky, 1989; Moore and Keller, 1991). Some rocks near the landers are meter-scale in size. For example, at the VL1 site there is a 2 m wide sediment-capped boulder named Big Joe within 10 m of the lander. Little is known about the composition or physical properties of rocks at the two landing sites. Despite several attempts, rock samples were never successfully collected for measurement by either lander's analytical instruments. However, rocks appear to be relatively strong, given that they were never chipped, scratched, or spalled while being pushed with the sampler arm or scraped by the backhoe. These observations also suggest that the rocks are not likely to have weak rinds (Moore *et al.*, 1987). It is estimated that rocks at the Viking sites have cohesions in the range of 10^3–10^4 kPa and angles of internal friction of 40°–60° based on analogy to crystalline terrestrial rocks (Moore *et al.*, 1987; Moore and Jakosky, 1989).

Similarly, rocks at the Mars Pathfinder landing site were never chipped nor scraped by rover wheels when driven onto or over during surface operations (see Chapter 21). The chemical composition of rocks analyzed by the Pathfinder Alpha Proton X-ray Spectrometer are all consistent with the rocks being dense, fine-grained volcanic rocks with weathering rinds or dust coatings (McSween *et al.*, 1999). Therefore, the physical properties of rocks at the Pathfinder landing site are similar to those estimated for rocks at the Viking landing sites (Moore and Jakosky, 1989).

As of early 2007, the MER RATs had been used to grind into 15 rocks in Gusev crater, and 30 rocks on Meridiani Planum (both outcrop and float; e.g., Figure 20.17). Energy expended during the deepest 0.25 mm of each grind can be calculated from instrument telemetry and compared with the volume removed. This calculation was used to obtain a measurement of each rock's resistance to grinding, which has been termed the "specific grind energy" (SGE; Myrick *et al.*, 2004):

$$\mathrm{SGE} = \frac{\mathrm{Energy}}{\mathrm{Volume}} = \frac{N\Delta t(\bar{I}_{\mathrm{grind}} - I_{\mathrm{noload}})V_{\mathrm{grind}}}{A_{\mathrm{abraded}}\Delta Z}, \qquad (20.1)$$

where N is the number of samples in the dataset, Δt is the sampling period, $\bar{I}_{\mathrm{grind}}$ is the mean current drawn by the grind motor, I_{noload} is an estimate of the current required to drive the mechanism without load, V_{grind} is the mean voltage applied to the grind motor, A_{abraded} is the grind area (measured from MI mosaics), and ΔZ is the overall change in depth across the dataset. Results from the *Spirit* rover are summarized in Table 20.3 and results from the *Opportunity* rover in Table 20.4.

Although SGE is not readily separated into constituent physical properties, initial investigations with testing on Earth indicated that grind energy is loosely correlated with unconfined compressive strength; rocks with higher grind energies typically have higher unconfined compressive strength (Myrick *et al.*, 2004). On Mars, the rocks that the *Spirit* RAT encountered at Gusev generally had much higher SGE values than the rocks that the *Opportunity* RAT encountered at Meridiani Planum.

Table 20.3. *Specific grind energy ($J\,mm^{-3}$) for rocks abraded by the* Spirit *RAT in Gusev crater*

Sol	Rock (target)	SGE
34	Adirondack (Prospect)	53.2
59	Humphrey (Heyworth)	49.2
81	Mazatzal (New York)	55.7
83	Mazatzal (Brooklyn)	49.7
195	Wooly Patch (Sabre)	5.15
198	Wooly Patch (Mastadon)	4.11
216	Clovis (Plano Spot)	8.26
231	Ebenezer (Cratchit 2)	8.92
285	Uchben (Koolik)	7.32
334	Wishstone (Chisel)	22.4
355	Champagne (Bubbles)	14.0
374	Peace (RAT Justice–1)	1.76
377	Peace (RAT Justice–2)	2.08
416	Watchtower (Joker)	30.6

Table 20.4. *Specific grind energy ($J\,mm^{-3}$) for rocks abraded by the* Opportunity *RAT in Meridiani Planum*

Sol	Rock (target)	SGE
30	McKittrick (Middle RAT)	1.67
34	Guadalupe (King 3)	46.2
44	Flatrock (Mojo 2)	1.14
66	Bouncerock (Case)	4.19
86	Pilbara (Golf)	1.25
107	Lion Stone (Puma)	18.1
138	Tennessee, a.k.a. Layer A (Vols)	0.332
143	Kentucky, a.k.a. Layer B (Cobble Hill)	1.41
145	Virginia, a.k.a. Layer C	0.775
148	London, a.k.a. Layer D, Ontario	0.183
151	Manitoba (Grindstone, a.k.a. Layer E1)	0.406
153	Manitoba (Kettlestone, a.k.a. Layer E2)	0.676
161	Millstone (Drammensfjord, a.k.a. Layer F)	0.145
177	Diamond Jenness (Holman 3–1)	0.149
178	Diamond Jenness (Holman 3–2)	−0.403
182	Mackenzie (Cambell 2)	−0.016
186	Inuvik (Tuktoyuktuk 2)	0.037
194	Bylot (Atkineq)	0.446
218	Escher (Kirchner)	4.69
311	Black Cow (Wharenhui)	0.567
402	Yuri (Gagarin)	1.22
545	IceCream (OneScoop)	0.683
558	FruitBasket(LemonRind)	0.507
633	Olympia (Kalavrita)	0.782
691	Rimrock (Ted)	0.928

However, the negative SGE values measured by *Opportunity* on Sol 178 and 182 highlight the practical uncertainties in SGE calculations from available telemetry; these uncertainties are present to some extent in all values of SGE. I_{noload} was calculated from postgrind RAT brushings (for those grind events which were immediately followed by a brushing, otherwise I_{noload} was estimated), and in this time period the grind motor and its transmission may have cooled sufficiently to increase the no-load current to the extent that it was larger than the grind current (on *Opportunity* Sols 178 and 182). Mechanism health otherwise may also affect SGE, as particulate matter caught in the seals of the RAT grind head may increase mechanical load and thus I_{noload}. Additionally, there is uncertainty regarding the forces at the grinding interface, where different rocks may provide different proportions of cutting and frictional resistance, when the cutting resistance is the only component that should be measured to assess rock grind energy.

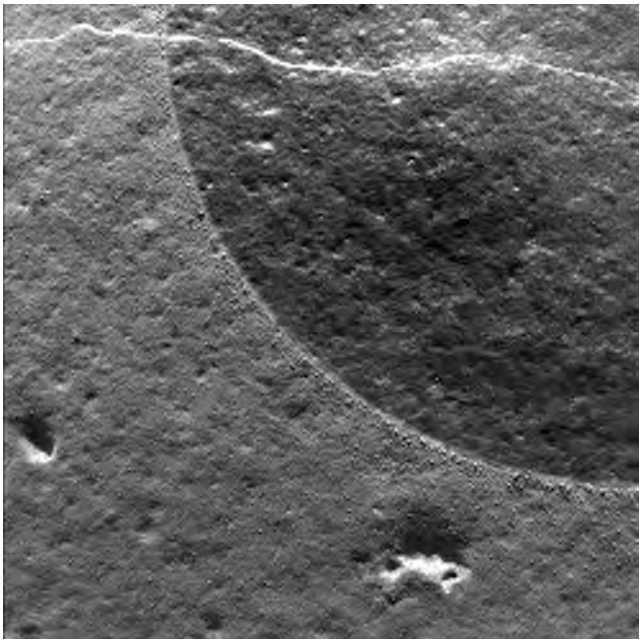

Figure 20.18. *Spirit* MI image 2M171727520IFFAAJCP2936M2F1 showing an area on the rock "Backstay" where RAT brushing of a dusty coating has occurred. Note that detailed rock relief is present in both brushed (darker) and unbrushed surfaces, implying that the dust coating is very thin ($\ll$ 1 mm). The image spans about 31 mm and was obtained on Sol 511 with illumination from the top. The dusty coating removed by the RAT brush appears to be ubiquitous in Gusev crater, and probably at many other places on Mars as well.

The grind energies required for abrading rocks at the Gusev crater and Meridiani sites can be compared to other chemical, mineralogical, and thermal data from the rovers to categorize their physical properties (summarized in Chapter 21). Extensive chemical composition and mineralogy investigations of rocks on the Gusev cratered plains indicate that they are olivine basalts with thin weathering rinds (McSween *et al.*, 2004). Gusev rock surfaces that have been brushed but not abraded by the RAT show evidence for a thin dust coating (Figure 20.18). Mini-TES measurements of thermal inertia are also high (Fergason *et al.*, 2006). These measurements suggest that Gusev plains rocks are fine-grained, dense volcanic rocks with high density, high cohesion, and high angle of internal friction (all of which are also consistent with the high grind energies [50–60] needed to abrade these rocks). Rocks in the Columbia Hills are mostly clastic rocks formed by volcanic or impact processes, with varying degrees of aqueous alteration (Squyres *et al.*, 2006). They have a different chemical composition and physical

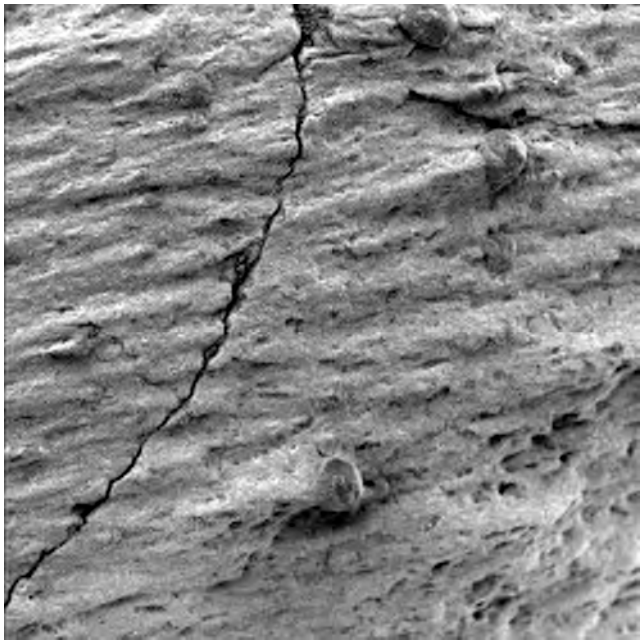

Figure 20.19. *Opportunity* MI image 1M162982683IFF4705P2977-M2F1 of sulfate-enriched bedrock abraded by wind-driven impacts of fine grains. The abrading grains were most likely similar to the ~100 μm mafic sand grains seen nearby (e.g., Figure 20.15). Hematite-enriched concretions are weathering out of this rock (~2 mm diameter examples are most obvious). The concretions are more resistant to abrasion, protecting streamlined "wind tails" of sulfate-enriched bedrock immediately downwind (toward left). This view is an example of the range of hardness of grains present in the same rock, revealed by differential erosion. The image is about 31 mm across, and was obtained on Sol 392 in the shadow of the instrument; diffuse illumination is from the top.

appearance than rocks observed on the plains, with lower Mini-TES thermal inertias and much lower grind energies of 2–24 J mm^{-3}. These results suggest that Columbia Hills rocks have reduced densities as well as cohesion and angle of internal friction compared with the denser volcanic rocks of the Gusev cratered plains. Layered evaporites at Meridiani Planum have very-low grind energies (0.1–2 J mm^{-3}), and the easily eroded nature of these outcrops by saltating basaltic sand suggests that they likely have even lower density and cohesion than the Columbia Hills rocks (Figure 20.19).

20.3 SUMMARY

Physical properties of Martian surface materials generally are not investigated as ends in themselves, but are evaluated to help address larger, science-driven questions or engineering needs. Soil and rock physical properties augment other information to help determine the origins and histories of surface materials, and can influence designs of future spacecraft mechanisms intended to interact with the Martian surface (e.g., landing systems, wheels, scoops, drills). For Viking, Pathfinder/Sojourner, and MER, the pursuit of this knowledge has been carried out according to the capabilities and limitations of each mission payload. These capabilities have changed dramatically from Viking to MER.

The Viking Landers, developed for investigating the possibility of life on Mars, were extremely ambitious machines for their time but had few tools for developing a "feel" for the surface materials at their landing sites. Compared with later missions, important limitations were lack of mobility, limited imaging resolution, and no capability for measurements below rock surfaces. Cameras could not resolve individual soil particles, so basic information on grain sizes, shapes, and sorting could not be measured. This was problematic in view of the significant aeolian-related bedforms observed at both sites. The unknown particle sizes of these bedforms left open questions about whether these features were composed of once-saltating, sand-sized grains, airfall dust, or a mixture (are they ripples, or dunes, or drift?). In the absence of definitive information, it was speculated that sand-sized grains might have short residence times on the Martian surface due to very high-speed saltation trajectories (Mutch *et al*., 1976; Sagan *et al*., 1977; Smalley and Krinsley, 1979; Sharp and Malin, 1984), and that if the aeolian features at the Viking sites were formed at least partly by saltation, grains of the expected saltation size might be assembled from smaller particles by electrostatic or other forces (Sagan *et al*., 1977; Greeley, 1979). The Viking surface sampler arms were too delicate to manipulate all but the weakest materials, allowing only approximate lower limits of rock hardness to be estimated. And without mobility, distinct soil units seen by the cameras out beyond the range of the sampler arm could not be investigated. Any additional nearby soil or rock units just out of view of the cameras at each site remained hidden.

Pathfinder/Sojourner offered improved capabilities for physical properties investigations, but in most respects the investigations were similar in approach to those of Viking. The Imager for Mars Pathfinder (IMP) had significantly greater spectral discriminability for identifying distinct soil, crust, and rock units (Smith *et al*., 1997), although resolution of individual soil grains still was not possible, leading to uncertainties about the nature and origin of the aeolian wind tails and bedforms observed there. Pathfinder had no sampler arm, but Sojourner rover wheel motor currents offered an analogous capability of inferring soil strength from electromechanical resistances. Unlike Viking, the Sojourner wheel/suspension system could be guided to different soil and crust targets over a larger area around the Pathfinder lander than could be reached by the Viking surface sampler arms. Sojourner was restricted to exploring only short distances from Pathfinder, however, but this was enough to reveal some terrain (including a different type of aeolian bedform) blocked from view of the lander (Matijevic *et al*., 1997; Rover Team, 1997). Like the Vikings, little could be measured or even inferred about hardness of the rocks at the Pathfinder landing site.

The two MER rovers have a much greater capability than previous missions for investigating soil and rock physical properties. Both MER vehicles are still operating as of this writing, and comprehensive analyses of physical properties

of materials encountered along each of their multikilometer traverses have not yet been completed. It is clear at this stage, however, that the greater capability of the MERs for determining physical properties has begun to change the way this information is pursued and considered. As with previous missions, the strength of soil and rock materials is estimated indirectly from current drawn by electric motors driving mechanisms in contact with surface materials; for MER, these mechanisms are the six wheels and the RAT. Similar to Pathfinder's Sojourner rover, motor currents during MER wheel digging activities have been analyzed to distinguish stronger soils from weaker soils. While the MER arm is a relatively delicate device unsuitable for scratching or impacting rock by its own motions, the RATs carried on these arms have revealed a wide range of resistances to grinding, with some correlation to rock type and degree of aqueous alteration. Variations in soil and rock strength revealed by each rover are more likely to be encountered and to be recognized over distances longer than the reach of a Viking sampler arm, or even the range of a Sojourner-class rover. This extended mobility of the MER vehicles, combined with much better imaging of tracks and airbag bounce/retraction marks than was possible with Pathfinder/Sojourner, has allowed more informative analysis of track and bounce/retraction mark morphology and sinkage, another indicator of soil strength and its variation at the landing sites and along traverses. However, the most significant improvement of MER over previous missions for assessing physical properties of materials is the capability to resolve fine particles and textural features with the MI. For the first time, sand-sized and larger soil grains can be resolved directly (although roundness and other shape properties are measurable only for the larger grains). One of the most significant discoveries regarding Martian soils and the role of wind currently shaping these deposits has been the direct imaging of sand-sized grains at both MER sites (even – perhaps surprisingly – on the rover deck, 66 cm above the surface), and their association with saltation of these grains to form the bedforms where they are found, helping to resolve uncertainties about particle movement on Mars (Greeley *et al*., 2004; Herkenhoff *et al*., 2004a,b; Sullivan *et al*., 2005).

20.4 FUTURE NEEDS AND DIRECTIONS

Uncertainties associated with determining some soil properties limit their usefulness in bounding engineering properties and geological processes. Actions that can be undertaken to reduce uncertainty in determining soil properties fall into three categories:

(1) Improve simulation models of machine/soil interactions.
(2) Design and fly instrumentation that directly measures load and torque during interactions with rocks and soil.
(3) Develop and deploy instruments specific to achieving soil study goals.

New approaches to simulating machine/soil interactions have been developed using the discrete (or distinct) element method (DEM) to represent granular media and soil particles (Tanaka *et al*., 2000; Momozua *et al*., 2003; Nakashima and Oida, 2004; Zhang and Li, 2006). These have been extended to analyze lunar microrover wheel performance (Nakashima *et al*., 2007) and to develop a simulation capability for the MER wheel (Figure 20.20). The DEM is a technique for explicitly modeling the dynamics of assemblies of particles and is useful when a material undergoes large-scale discontinuous deformations that depend on micro-scale contact processes, internal breakage of contact bonds, and compaction of broken fragments (Cundall and Strack, 1979; Hopkins, 2004; Johnson and Hopkins, 2005). The simulations of DEM are numerical experiments of complex machine/soil interactions that can be compared to measured forces and observed three-dimensional soil deformation.

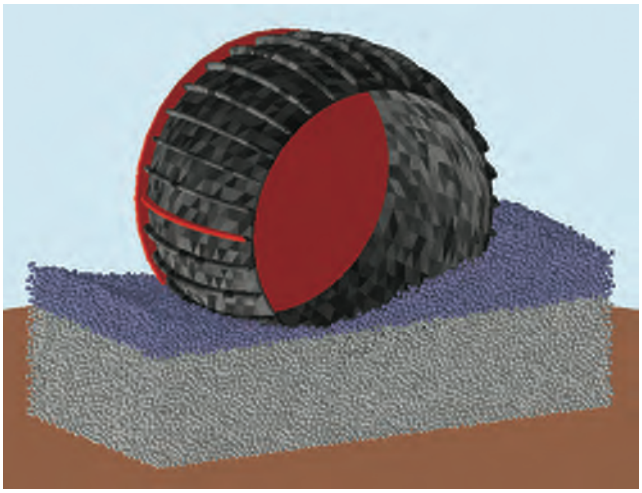

Figure 20.20. Discrete Element Method (DEM) computer simulation of an MER wheel digging in soil. (For a color version of this figure, please refer to the color plate section or to the e-Book version of this chapter.)

Equipment modifications to reduce uncertainty in determining Mars soil strength and heterogeneity consist primarily of adding force and torque sensors to wheels and probes to allow higher resolution measurements during interactions with soil. For example, the addition of a ranging/motion laser pointed toward ground next to a wheel would allow direct measurement of rover velocity, and wheel slip and sinkage during travel or during wheel trenching operations. Such additions, and wheel rotation monitoring, could allow the robot wheel to act as a mobile terrain characterization tool (Iagnemma *et al*., 2004; Ojeda *et al*., 2005) to estimate soil strength and its variation. Wheel force and torque measurements can also be used to implement optimizing criteria to minimize the occurrence of terrain failure and gross wheel slip, by monitoring the ratio of wheel tractive force (torque) to the normal force (Iagnemma and Dubowsky, 2004). Terrain failure detection methods that compare wheel and rover speeds could be used, for example, to prevent rover embedment from occurring. The addition of force sensors to scoops or other objects pressed into the soil could provide additional machine/soil data at higher resolution than is currently achieved by analyzing machine motor currents for later analysis and simulation.

Surface and subsurface access could be achieved using a dedicated instrumented digging bucket or an instrumented penetrometer. An instrumented digging bucket could serve dual purposes of digging trenches to expose soil layers to rover instruments and acting as a platform for soil properties measurement tools. These tools could include, for example, two force-sensitive indenters of different areas for pressure/sinkage measurements, a force-sensitive skid plate to measure soil/metal friction and abrasion, and a direct shear blade to measure soil strength. With some creative design, the bucket could apply varying normal loads during shear tests to determine both soil internal friction and cohesion.

An instrumented penetrometer might consist of a cone mounted on a hollow rod that is pushed or hammered into the soil. Instruments or fiber optics that transmit laser light to interrogate soil properties could be inserted into the core of the rod. The depth of penetration and the force, momentum, or energy required to insert the penetrometer into the soil could be measured to estimate soil strength, layering, compaction, and density. Instruments to measure density, mineralogy, grain size and shape, and texture as a function of depth have been developed for both Earth and space applications (e.g., Ball *et al.*, 1998, 2001; Lieberman and Knowles, 1998; Rossabi *et al.*, 2000; Mungas *et al.*, 2007). A penetrometer could also make bevameter-like measurements of steel/soil friction and shear strength by using in-line cone sections. The lower section could be smooth and rotate, providing a friction versus normal load measurement. The upper section could contain shear vanes that would produce a shear failure in the soil when rotated (Garciano *et al.*, 2006). Self-propelled penetrometers are devices equipped with an internal hammering mechanism that transfers the recoil force to the medium surrounding the penetrometer. One such instrument has already been developed for flight (Richter *et al.*, 2002) and instrumented ones are currently under technology development (e.g., Stoker *et al.*, 2003).

REFERENCES

Arvidson, R. E., J. L. Gooding, and H. J. Moore, The martian surface as imaged, sampled and analyzed by the Viking Landers, *Rev. Geophys.* **27**, 39–60, 1989.

Arvidson, R. E., R. C. Anderson, A. F. C. Haldemann, *et al.*, Physical properties and localization investigations associated with the 2003 Mars Exploration Rovers, *J. Geophys. Res.* **108** (E12), 8070, doi:10.1029/2002JE002041, 2003.

Arvidson, R. E., R. C. Anderson, P. Bartlett, *et al.*, Localization and physical properties experiments conducted by Spirit at Gusev crater, *Science* **305**, 821–4, 2004a.

Arvidson, R. E., R. C. Anderson, P. Bartlett, *et al.*, Localization and physical properties experiments conducted by Opportunity at Meridiani Planum, *Science* **306**, 1730–3, 2004b.

Ball, A. J., C. J. Solomon, and J. C. Zarnecki, The response of gamma backscatter density gauges to spatial inhomogeneity: an extension of the single scattering model, *Nucl. Instrum. Meth. Phys. Res. B* **140**(3/4), 449–62, 1998.

Ball, A. J., S. Gadomski, M. Banaszkiewicz, *et al.*, An instrument for in situ comet nucleus surface density profile measurement by gamma ray attenuation, *Planet. Space Sci.* **49**(9), 961–76, 2001.

Bell III, J. F., S. Squyres, K. Herkenhoff, *et al.*, Mars Exploration Rover Athena Panoramic Camera (Pancam) investigation, *J. Geophys. Res.* **108**(E12), 8063, doi:10.1029/2003JE002070, 2003.

Binder, A. B., R. E. Arvidson, E. A. Guinness, *et al.*, The geology of the Viking Lander 1 site, *J. Geophys. Res.* **82**, 4439–51, 1977.

Carrier III, W. D., G. R. Olhoeft, and W. Mendell, Physical properties of the lunar surface. In *Lunar Sourcebook* (ed. G. H. Heiken, D. T. Vaniman, and B. M. French), Cambridge University Press, pp. 475–594, 1991.

Christensen, P. R., The spatial distribution of rocks on Mars, *Icarus* 68, 217–38, 1986.

Christensen, P. R. and H. J. Moore, The Martian surface layer. In *Mars* (ed. H. H. Kieffer, B. M. Jakosky, C. W. Snyder, and M. S. Matthews), Tucson: University of Arizona Press, pp. 686–727, 1992.

Christensen, P. R., G. L. Mehall, S. H. Silverman, *et al.*, Miniature thermal emission spectrometer for the Mars Exploration Rovers, *J. Geophys. Res.* **108** (E12), 8064, doi:10.1029/2003JE002117, 2003.

Clark, B. C., A. K. Baird, H. J. Rose Jr., *et al.*, The Viking X-ray fluorescence experiment: analytical methods and early results, *J. Geophys. Res.* **82**, 4577–94, 1977.

Clark, B. C., A. K. Baird, R. J. Weldon, *et al.*, Chemical composition of martian fines, *J. Geophys. Res.* **87**, 10059–67, 1982.

Cundall, P. A. and O. D. L. Strack, A discrete numerical model for granular assemblies, *Geotechnique* **29**, 47–65, 1979.

Evans, J. V. and T. Hagfors, *Radar Astronomy*, New York: McGraw-Hill, 620pp., 1968.

Fergason, R. L., P. R. Christensen, J. F. Bell III, *et al.*, Physical properties of the Mars Exploration Rover landing sites as inferred from Mini-TES derived thermal inertia, *J. Geophys. Res.* **111**(E2), E02S21, doi:10.1029/2005JE002583, 2006.

Ferguson, D. C., J. C. Kolecki, M. W. Siebert, D. M. Wilt, and J. R. Matijevic, Evidence for martian electrostatic charging and abrasive wheel wear from wheel abrasion experiment on the Pathfinder Sojourner rover, *J. Geophys. Res.* **104**, 8747–89, 1999.

Garciano, L. O., S. K. Upadhyaya, R. A. Jones, and S. R. Jersy, *Development of an Instrumented Portable Device that Measures Shear, Sinkage and Friction Properties of Soil in-situ*, American Society of Agricultural and Biological Engineers meeting presentation paper No. 061093, 14pp., 2006.

Golombek, M. P., and the Mars Pathfinder science team, Overview of the Mars Pathfinder mission: launch through landing, surface operations, data sets, and science results, *J. Geophys. Res.* **104**, 8523–53, 1999a.

Golombek, M. P., H. J. Moore, A. F. C. Haldemann, T. J. Parker, and J. T. Schofield, Assessment of Mars Pathfinder landing site predictions, *J. Geophys. Res.* **104**, 8585–94, 1999b.

Golombek, M. P., A. F. C. Haldemann, N. K. Forsberg-Taylor, *et al.*, Rock size-frequency distributions on Mars and implications for MER landing safety and operations, *J. Geophys. Res.* **108**(E12), 8086, doi:10.1029/2002JE002035, 2003.

Golombek, M. P., R. E. Arvidson, J. F. Bell III, *et al.*, Assessment of Mars Exploration Rover landing site predictions, *Nature* **436**, 44–8, 2005.

Gorevan, S. P., T. Myrick, K. Davis, *et al.*, Rock Abrasion Tool: Mars Exploration Rover mission, *J. Geophys. Res.* **108**, 8068, doi:10.129/2003JE002061, 2003.

Greeley, R., Silt-clay aggregates on Mars, *J. Geophys. Res.* **84**, 6248–54, 1979.

Greeley, R., M. Kraft, R. Sullivan, *et al*., Aeolian features and processes at the Mars Pathfinder landing site, *J. Geophys. Res*. **104**, 8573–84, 1999.

Greeley, R., M. D. Kraft, R. O. Kuzmin, and N. T. Bridges, Mars Pathfinder landing site: evidence for a change in wind regime and climate from lander and orbiter data, *J. Geophys. Res*. **105**, 1829–40, 2000.

Greeley, R., S. W. Squyres, R. E. Arvidson, *et al*., Wind-related processes detected by the Spirit rover at Gusev crater, Mars, *Science* **305**, 810–21, 2004.

Hagfors, T., Backscattering from an undulating surface with applications to radar returns from the Moon, *J. Geophys. Res*. **69**, 3779–84, 1964.

Herkenhoff, K. E., S. W. Squyres, J. F. Bell III, *et al*., Athena Microscopic Imager investigation, *J. Geophys. Res*. **108**, 8065, doi:10.1029/2003JE002076, 2003.

Herkenhoff, K. E., S. W. Squyres, R. Arvidson, *et al*., Textures of the soils and rocks at Gusev crater from Spirit's Microscopic Imager, *Science* **305**, 824–6, 2004a.

Herkenhoff, K. E., S. W. Squyres, R. Arvidson, *et al*., Evidence for ancient water on Meridiani Planum from Opportunity's Microscopic Imager, *Science* **306**, 1727–30, 2004b.

Hopkins, M. A., Discrete element modeling with dilated particles, *J. Eng. Comput*. **21**(2), 422–30, doi:10.1108/02644400410519866, 2004.

Huck, F. O., H. F. McCall, W. R. Patterson, and G. R. Taylor, The Viking Mars lander camera, *Space Sci. Instrum*. **1**, 189–241, 1975.

Iagnemma, K. and S. Dubowsky, Traction control of wheeled robotic vehicles in rough terrain with application to planetary rovers, *Int. J. Robot. Res*. **23**, 1029–40, doi:10.1177/0278364904047392, http://ijr.sagepub.com/cgi/content/abstract/23/10-11/1029, 2004.

Iagnemma, K., S. Kang, H. Shibly, and S. Dubowsky, On-line terrain parameter estimation for planetary rovers, *IEEE Trans. Robot*., **20**(2), 921–7, 2004.

Jerolmack, D. J., D. Mohrig, J. P. Grotzinger, D. A. Fike, and W. A. Watters, Spatial grain size sorting in eolian ripples and estimation of wind conditions on planetary surfaces: application to Meridiani Planum, Mars. *J. Geophys. Res*. **111**, E12S02, doi:10.1029/2005JE002544, 2006.

Johnson, J. B. and M. A. Hopkins, Identifying microstructural deformation mechanisms in snow using discrete element modeling, *J. Glaciology* **51**, 432–42, 2005.

Kemurdzhian, A. L., O. G. Ivanov, P. S. Pavlov, *et al*., The self-propelled chassis of Lunokhod-1 as an instrument for investigating the lunar surface. In *Mobile Laboratory on the Moon* (ed. V. L. Barsukov), Lunokhod-1, Moscow: Nauka, Vol. 2, pp. 25–66, 1978.

Kieffer, H. H., T. Z. Martin, A. R. Peterfreund, *et al*., Thermal and albedo mapping of Mars during the Viking Primary Mission, *J. Geophys. Res*. **82**, 4249–91, 1977.

Klingelhöfer, G., R. V. Morris, B. Bernhardt, *et al*., Athena MIMOS II Mössbauer spectrometer investigation, *J. Geophys. Res*. **108**, 8067, doi:10.1029/2003JE002138, 2003.

Lieberman, S. H. and D. S. Knowles, Cone penetrometer deployable *in situ* video microscope for characterizing sub-surface soil properties, *Field Analyt. Chem. & Technol*. **2**(2), 127–32, 1998.

Maki, J. N., J. F. Bell III, K. E. Herkenhoff, *et al*., The Mars Exploration Rover engineering cameras, *J. Geophys. Res*. **108**, doi:10.1029/2003JE002077, 2003.

Matijevic, J. R., J. Crisp, D. B. Bickler, *et al*., Characterization of the Martian surface deposits by the Mars Pathfinder rover, Sojourner, *Science* **278**, 1765–8, 1997.

McLane, M., *Sedimentology*, New York: Oxford University Press, 1995.

McSween Jr., H. Y., S. L. Murchie III, D. T. Britt, *et al*., Chemical, multispectral, and textural constraints on the composition and origin of rocks at the Mars Pathfinder landing site, *J. Geophys. Res*. **104**, 8679–716, doi:10.1029/98JE02551, 1999.

McSween, H. Y., R. E. Arvidson, J. F. Bell III, *et al*., Basaltic rocks analyzed by the Spirit rover in Gusev crater, *Science* **305**, 842–5, 2004.

Mitchell, J. K., W. N. Houston, R. F. Scott, *et al*., Mechanical properties of lunar soils: density, porosity, cohesion, and angle of internal friction, *Proc. Lunar Sci. Conf. III, Sup. 3, Geochim. Cosmochim. Acta* **3**, 3235–53, 1972.

Momozua, M., A. Oidaa, M. Yamazakib, and A. J. Koolenc, Simulation of a soil loosening process by means of the modified distinct element method, *J. Terramechanics* **39**, 207–20, 2003.

Moore, H. J. and B. M. Jakosky, Viking landing sites, remote-sensing observations, and physical properties of martian surface materials, *Icarus* **81**, 164–84, 1989.

Moore, H. J. and J. M. Keller, Surface-material maps of Viking landing sites on Mars, *Reports of Planetary Geology and Geophysics Program – 1990*, NASA Technical Memorandum **4300**, 160–2, 1991.

Moore, H. J., R. E. Hutton, R. F. Scott, C. R. Spitzer, and R. W. Shorthill, Surface materials of the Viking landing sites, *J. Geophys. Res*. **82**, 4497–523, 1977.

Moore, H. J., C. R. Spitzer, K. Z. Bradford, *et al*., Sample fields of the Viking landers, physical properties, and aeolian processes, *J. Geophys. Res*. **84**, 8365–77, 1979.

Moore, H. J., G. D. Clow, and R. E. Hutton, A summary of Viking sample-trench analyses for angles of internal friction and cohensions, *J. Geophys. Res*. **87**, 10043–50, 1982.

Moore, H. J., R. E. Hutton, G. D. Clow, and C. R. Spitzer, *Physical Properties of the Surface Materials of the Viking Landing Sites on Mars*, *USGS Prof*. Paper, 1389, 222pp., 1987.

Moore, H. J., D. Bickler, J. Crisp, *et al*., Soil-like deposits observed by Sojourner, the Pathfinder rover, *J. Geophys. Res*. **104**, 8729–46, 1999.

Mungas, G., C. Sepulveda, K. Johnson, *et al*., *Raman/CHAMP Instrument for Lunar in-situ Resource Prospecting I–Imager Design*, IEEEAC paper #1554, 2007.

Mutch, T. A., R. E. Arvidson, A. B. Binder, *et al*., Fine particles on Mars: observations with the Viking 1 Lander cameras, *Science* **194**, 87–91, 1976.

Mutch, T. A., R. E. Arvidson, A. B. Binder, E. A. Guinness, and E. C. Morris, The geology of the Viking Lander 2 site, *J. Geophys. Res*. **82**, 4452–67, 1977.

Myrick, T. M., P. Bartlett, L. Carlson, *et al*., The RAT as a Mars Rock Physical Properties Tool, *Space 2004 Conference and Exhibit*, San Diego, CA, AIAA-2004–6096, American Institute of Aeronautics and Astronautics, Reston, VA, September 28–30, 2004.

Nakashima, H. and A. Oida, Algorithm and implementation of soil–tire contact analysis code based on dynamic FE–DE method, *J. Terramechanics* **41**, 127–37, 2004.

Nakashima, H., H. Fujii, A. Oida, *et al*., Parametric analysis of lugged wheel performance for a lunar microrover by means of DEM, *J. Terramechanics* **44**, 153–62, 2007.

Ojeda, L., J. Borenstein, and G. Witus, Terrain trafficability characterization with mobile robot, *Proc. SPIE Defense and Security Conf., Unmanned Ground Vehicle Technology VII*, Orlando, FL, March 28–April 1, 2005.

Olhoeft, G. R. and D. W. Strangway, Dielectrical properties of the first 100 meters of the Moon, *Earth Planet. Sci. Lett.* **24**, 394–404, 1975.

Presley, M. A. and P. R. Christensen, Thermal conductivity measurements of particulate materials: 2. Results, *J. Geophys. Res.* **102**, 6551–66, 1997.

Richter, L., P. Coste, V. V. Gromov, *et al.*, Development and testing of subsurface sampling devices for the Beagle 2 lander, *Planet. Space Sci.* **50**, 903–13, 2002.

Richter, L., A. Ellery, Y. Gao, *et al.*, A predictive wheel-soil interaction model for planetary rovers validated in testbeds and against MER Mars Rover performance data, *Proc. 10th European Conf. Int. Soc. Terrain-Vehicle Systems (ISTVS)*, Budapest, October 3–6, 2006.

Rieder, R., R. Gellert, R. C. Anderson, *et al.*, Chemistry of rocks and soils at Meridiani Planum from the Alpha Particle X-ray Spectormeter, *Science* **306**, 1746–9, 2004.

Rossabi, J., B. D. Riha, J. W. Haas, *et al.*, Field tests of a DNAPL characterization system using cone penetrometer-based Raman spectroscopy, *Ground Water Monit. Rem.* **20**(4), 72–81, 2000.

Rover Team, The Pathfinder microrover, *J. Geophys. Res.* **102**, 3989–4001, 1997.

Sagan, C., D. Pieri, P. Fox, R. E. Arvidson, and E. A. Guinness, Particle motion on Mars inferred from the Viking Lander cameras, *J. Geophys. Res.* **82**, 4430–8, 1977.

Sharp, R. P. and M. C. Malin, Surface geology from Viking landers on Mars: a second look, *Geol. Soc. Am. Bull.* **95**, 1398–412, 1984.

Smalley, I. J. and D. H. Krinsley, Eolian sedimentation on Earth and Mars: some comparisons, *Icarus* **40**, 276–88, 1979.

Smith, P., M. Tomasko, D. Britt, *et al.*, The imager of Mars Pathfinder experiment, *J. Geophys. Res.* **102**, 4003–25, 1997.

Soderblom, L. A., R. C. Anderson, R. E. Arvidson, *et al.*, Soils of Eagle crater and Meridiani Planum at the Opportunity rover landing site, *Science* **306**, 1723–6, 2004.

Squyres, S. W., R. E. Arvidson, D. L. Blaney, *et al.*, Rocks of the Columbia Hills, *J. Geophys. Res.* **111**, E02S11, doi:10.1029/2005JE002562, 2006.

Stoker, C. R., L. Richter, W. H. Smith, *et al.*, The Mars Underground Mole (MUM): a subsurface penetration device with in situ infrared reflectance and Raman spectroscopic sensing capability, *6th Int. Mars Conf.*, Abstract #3007, 2003.

Sullivan, R., D. Banfield, J. F. Bell III, *et al.*, Aeolian processes at the Mars Exploration Rover Meridiani Planum landing site, *Nature* **436**, 58–61, 2005.

Tanaka, H., M. Momozua, A. Oida, and M. Yamazaki, Simulation of soil deformation and resistance at bar penetration by the Distinct Element Method, *J. Terramechanics* **37**, 41–56, 2000.

Wänke, H., J. Brückner, G. Dreibus, R. Rieder, and I. Ryabchikov, Chemical composition of rocks and soils at the Pathfinder site, *Space Sci. Rev.* **96**, 317–30, 2001.

Weitz, C. M., R. C. Anderson, J. F. Bell III, *et al.*, Soil grain analyses at Meridiani Planum, Mars, *J. Geophys. Res.* **111**, E12S04, doi:10.1029/2005JE002541, 2006.

Zhang, R. and J. Li, Simulation on mechanical behavior of cohesive soil by distinct element method, *J. Terramech.* **43**, 303–16, 2006.